The Atmospheric Radiation Measurement Program Cloud Profiling Radars: An Evaluation of Signal Processing and Sampling Strategies

PAVLOS KOLLIAS,* EUGENE E. CLOTHIAUX,+ BRUCE A. ALBRECHT,* MARK A. MILLER,#
KENNETH P. MORAN,@ AND KAREN L. JOHNSON#

*Rosenstiel School of Marine and Atmospheric Science, University of Miami, Coral Gables, Florida
+Department of Meteorology, The Pennsylvania State University, University Park, Pennsylvania
#Division of Applied Sciences, Brookhaven National Laboratory, Upton, New York
@NOAA/Environmental Technology Laboratory, Boulder, Colorado

(Manuscript received and in final form 5 November 2004)

ABSTRACT

The U.S. Department of Energy (DOE) Atmospheric Radiation Measurements (ARM) program operates millimeter-wavelength cloud radars (MMCRs) in several specific locations within different climatological regimes. These vertically pointing cloud profiling radars supply the three most important Doppler spectrum moment estimates, which are the radar reflectivity (or zero moment), the mean Doppler velocity (or first moment), and the Doppler spectrum width (or second moment), as a function of time and height. The ARM MMCR Doppler moment estimates form the basis of a number of algorithms for retrieving cloud microphysical and radiative properties. The retrieval algorithms are highly sensitive to the quality and accuracy of the MMCR Doppler moment estimates. The significance of these sensitivities should not be underestimated, because the inherent physical variability of clouds, instrument-induced noise, and sampling strategy limitations all potentially introduce errors into the Doppler moment estimates. In this article, the accuracies of the first three Doppler moment estimates from the ARM MMCRs are evaluated for a set of typical cloud conditions from the three DOE ARM program sites. Results of the analysis suggest that significant errors in the Doppler moment estimates are possible in the current configurations of the ARM MMCRs. In particular, weakly reflecting clouds with low signal-to-noise ratios (SNRs), as well as turbulent clouds with nonzero updraft and downdraft velocities that are coupled with high SNR, are shown to produce degraded Doppler moment estimates in the current ARM MMCR operational mode processing strategies. Analysis of the Doppler moment estimates and MMCR receiver noise characteristics suggests that the introduction of a set of quality control criteria is necessary for identifying periods of degraded receiver performance that leads to larger uncertainties in the Doppler moment estimates. Moreover, the temporal sampling of the ARM MMCRs was found to be insufficient for representing the actual dynamical states in many types of clouds, especially boundary layer clouds. New digital signal processors (DSPs) are currently being developed for the ARM MMCRs. The findings presented in this study will be used in the design of a new set of operational strategies for the ARM MMCRs once they have been upgraded with the new DSPs.

1. Introduction

During the past decade, the U.S. Department of Energy (DOE), through the Atmospheric Radiation Measurement (ARM) program (Stokes and Schwartz 1994; Ackerman and Stokes 2003), supported the development and deployment of several millimeter-wavelength cloud radars (MMCRs) for the study of clouds. The MMCRs are deployed at sites in the Southern Great Plains (SGP) of Oklahoma, the North Slope of Alaska (NSA), and the tropical western Pacific (TWP). The MMCRs, together with the micropulse lidar (MPL; Spinhirne et al. 1989), are the primary observing tools for quantifying the properties of nearly all radiatively important clouds over the ARM sites. This includes a wide range of cloud types, from shallow fair-weather cumulus and stratus in the boundary layer to thin cirrus and convective anvils in the upper troposphere. The ARM MMCRs have been designed to provide accurate radar reflectivity measurements over a dynamic range

Corresponding author address: Dr. Pavlos Kollias, Division of Meteorology and Physical Oceanography, Rosenstiel School of Marine and Atmospheric Science, University of Miami, 4600 Rickenbacker Causeway, Miami, FL 33149.
E-mail: pkollias@rsmas.miami.edu

from approximately −50 to +20 dBZ, which has not been attempted before by a single research radar.

The Environmental Technology Laboratory (ETL) of the National Oceanic and Atmospheric Administration (NOAA) undertook the task of building the MMCRs (Moran et al. 1998) and developing an operational scheme (Clothiaux et al. 1999) to meet the objectives set by the ARM Program. The MMCRs have now been operating at the ARM sites for several years [i.e., since 8 November 1996, 6 November 1998, 1 November 1998, 1 August 1999, and 1 March 2002 at the SGP, NSA, TWP site at Nauru (TWP-Nauru), TWP site at Manus, Papua New Guinea (TWP-Manus), and TWP site at Darwin, Australia (TWP-Darwin), respectively], and have exhibited fair operational stability, providing long-term statistics of cloud boundaries, cloud types, and cloud reflectivities along with mean Doppler velocities and Doppler spectrum widths. The need to detect clouds with reflectivities below −40 dBZ at different altitudes dictates the use of different operational modes for the radar that can be cycled through repetitively. Some modes use pulse compression techniques with long pulses to boost radar sensitivity, allowing for the detection of weakly reflecting clouds, while other modes use conventional short pulses. Each mode involves trade-offs among sensitivity, spatial resolution, temporal resolution, velocity aliasing, range aliasing, and range sidelobe artifacts.

Since the deployment of the first MMCR at the SGP site, our understanding of nonprecipitating clouds has advanced (e.g., Kollias et al. 2001; Vali et al. 1998; Kato et al. 2001; Sassen et al. 1999; Mace et al. 2001; Dong and Mace 2003a). While providing cloud microphysical and dynamical state information to cloud (e.g., Luo et al. 2003) and radiative transfer (e.g., Dong and Mace 2003b) modelers is an important observational goal, such information is also important for accurate cloud detection by the radar in the first place. For example, clouds are highly inhomogeneous and turbulent (e.g., Kollias and Albrecht 2000), and the radar signal bandwidth must be sufficiently broad to record with fidelity return signals from them. Using case studies and a compilation of Doppler moment statistics from the MMCRs, we now evaluate the ARM MMCR performance.

To this end, data from the ARM SGP, NSA, and TWP sites are analyzed and MMCR signal characteristics and statistics are computed. In particular, we used the signal and noise statistics to compute means and variances for the Doppler moment estimates. Numerical simulations of radar signals for conditions based on the case study MMCR data were then performed. Theoretical estimates of MMCR cloud reflectivity, mean Doppler velocity, and Doppler spectrum width, especially at low signal-to-noise ratio (SNR) conditions, were obtained from the simulation outputs. The influence of the current operational parameters of each MMCR mode on data quality is investigated, together with the effects of the MMCR low temporal resolution sampling on derived cloud properties. Currently, an upgrade of the MMCR digital signal processor (DSP) is under way. This evaluation of the performance and efficiency of the current radar operational modes will provide invaluable input to the design of the new operational modes for these processors.

2. Background

The ARM MMCR is a vertically pointing, cloud-profiling system that operates at 35-GHz (i.e., Ka band) frequencies, which correspond to 8.7-mm wavelengths. The only other prevalent cloud-profiling radar frequency is at 94-GHz (i.e., W band) frequencies, which correspond to 3.2-mm wavelengths (e.g., Lhermitte 1987). Millimeter-wavelength radars are ideal for the detection of weakly reflecting meteorological targets, such as warm clouds composed of small cloud droplets. Their excellent sensitivity results from the proportionality of the backscattering cross section to $1/\lambda^4$ (i.e., Rayleigh scattering), where λ is the radar wavelength. Along with the inherent gain as a result of their short wavelength, the hardware design of the MMCRs was optimized for maximum sensitivity, including the choice of antenna size, receiver bandwidth, and electronics. The selection of a low-power traveling wave tube amplifier (TWTA) as transmitter was a compromise between average power, operational stability, and long lifetime.

The MMCRs use a phase-coded pulse compression technique (e.g., Schmidt et al. 1979) that boosts radar sensitivity by 10–15 dB over a conventional short-pulse radar. In the ARM MMCR nomenclature the number of coded bits (N_{bits}) is used to characterize the length and gain of a long MMCR phase-coded pulse relative to the pulse width (τ_{pw}). Another method for improving radar sensitivity is signal integration. Because the ARM MMCRs operate in a vertically pointing mode, their range of detection is 15–20 km with a pulse repetition frequency (PRF) as high as 10 kHz, depending on the transmitter duty cycle. Thus, a large number of samples is available each second. Unfortunately, the current MMCR DSPs have limited capabilities and duty cycles. The problem is partially overcome with the use of coherent integration, which is the averaging of N_{ci} consecutive radar pulse returns. The technique reduces the data volume by N_{ci} and, under certain conditions, leads to an increase in radar sensitivity. Other important pa-

TABLE 1. General characteristics of the current operational modes for the ARM program MMCRs.

Mode	MMCR			
	Boundary layer	Cirrus	General	Robust
Minimum range (R_{min}, km)	0.5	3.0	0.1	0.1
Maximum range (R_{max}, km)	5–6	13–20	13–20	13–20
Range volume spacing (R_{space}, m)	45	90	90	45–90
Number-coded bits (N_{bits})	8	32	0	0
Number coherent averages (N_{coh})	8–10	4–6	5–7	1
Unambiguous velocity (V_u, m s^{-1})	3.0–3.2	2.8–3.4	3.0–3.2	12–20
No. of samples (kHz)	25–40	4–8	14–31	3.5–5.0
DSP efficiency (%)	25–54	2.3–7.0	8.5–29.0	1.6–5.0

rameters of MMCR signal processing are the number of spectra averaged (N_{spec}), the number of fast Fourier transform (FFT) points (N_{fft}), and the Nyquist velocity (V_{ny}), which is a function of the radar wavelength λ, radar PRF, and N_{ci} through the equation

$$V_{ny} = \frac{\text{PRF}\lambda}{4N_{ci}}. \quad (1)$$

Given the above-mentioned tunable radar parameters, MMCR sensitivity can be optimized for certain applications. The ARM program requirement for the detection of all clouds with reflectivities from −50 to +20 dBZ is a difficult task, leading to the development of multiple operational modes. At the ARM program sites the MMCR cycles through a sequence of four operating modes that have differing sensitivities, height coverages, and resolutions. Detailed descriptions of the MMCR radars and their operating characteristics can be found in Moran et al. (1998) and Clothiaux et al. (1999, 2000). The four modes, each with a temporal resolution of 9 s, are a "boundary layer mode" (mode 1), suitable for the detection of low-level clouds, especially liquid phase stratus and fair-weather cumulus clouds; a "cirrus mode" (mode 2), tuned for the detection of thin upper-troposphere ice clouds; a "general mode" (mode 3), with high sensitivity at all altitudes; and a "robust mode" (mode 4), with a wide signal bandwidth that saturates only in moderately precipitating conditions (15 dBZ at 1 km). The general characteristics of the operational modes that are useful in our analysis are summarized in Table 1.

The MMCR operational modes were designed to boost radar sensitivity and allow for the detection of weakly reflecting clouds. Every parameter setting comes at the expense of radar artifacts, Doppler moment estimate errors, or biases, and resolution degradation. For example, the use of pulse compression comes at the expense of range sidelobe artifacts, which may contaminate data in the vicinity of stronger echoes, and a higher minimum useable altitude because of incomplete phase decoding in the first $N_{bits} - 1$ range gates. Additionally, the use of coherent integration comes at the expense of narrow Nyquist velocities V_{ny} [Eq. (1)]. For the modes now in operation a selection of the Nyquist velocities was based on particle (e.g., small cloud droplets and ice crystals) terminal fall velocities. However, in the presence of updrafts and downdrafts, vertical air motion is the primary contributor to the observed Doppler velocities, and the air motion vertical speeds often approach, or exceed, the Nyquist velocity, causing velocity folding. In the case of velocity folding, the accuracy of all three Doppler moments is degraded by filtering associated with coherent integration.

The current operational modes are temporally spaced by 9 s as a result of limited DSP speed and the need for significant signal integration to improve radar sensitivity. The temporal and spatial resolutions of the current modes are illustrated in Fig. 1. The cirrus and boundary layer modes cover only part of the atmospheric column from the surface to the top of the troposphere. A sequence of the four operational modes takes 36 s, and only three Doppler moment estimates are available in the boundary layer and at cirrus altitudes. Clothiaux et al. (2000) developed a methodology to identify significant returns in the MMCR data and, thereby, ascertained the distribution of the hydrometeors in the vertical column above the ARM sites. Significant Doppler moment estimates from the different modes are merged into a single time series. However, the relatively poor temporal resolution of the ARM MMCRs (Fig. 1) makes the resulting cloud composite image blocky, especially for vertically thin and weakly reflecting clouds, like boundary layer fair weather cumulus.

During data acquisition, the radar DSP acquires N_{fft} radar samples and calculates the Doppler power density spectrum for each radar range gate. This procedure is repeated N_{spec} times within the 9-s period that is devoted to each radar mode with temporal gaps between each of the N_{spec} spectra (Fig. 1). The DSP effi-

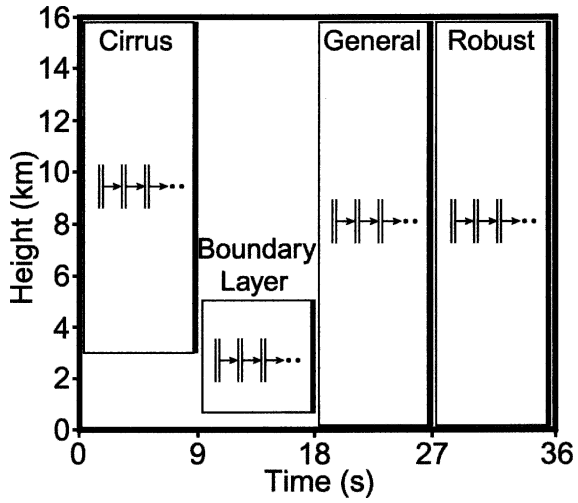

FIG. 1. Temporal and spatial coverage of the current MMCR operational modes. The collection of pulses by the ARM MMCR DSPs for the generation of each Doppler spectrum is indicated by the pairs of short vertical lines. Note that many radar pulses go unused and that the final Doppler spectrum generated at the end of the 9-s data collection period is an average of all of the Doppler spectra indicated by the pairs of short vertical lines. As such, the Doppler spectra generated by the ARM MMCRs contain contributions smeared out over the 9-s interval.

ciency parameter (Table 1) shows the fraction of the radar pulses over the 9 s that are actually used for the estimation of the Doppler spectrum. This discontinuous radar data acquisition technique is imposed by DSP limitations and has no, or little, effect on the Doppler moment estimates if the cloud microphysical and dynamical states are stationary within the signal dwell and processing (SDP) period. Recent observations (e.g., Kollias and Albrecht 2000) have demonstrated that this is not true, in general. Thus, the discontinuous 9-s SDP period filters the radar-derived cloud properties, including cloud boundaries, cloud liquid water content (LWC), cloud ice water content (IWC), and in-cloud turbulence. The reflectivity data, in particular, are fundamental to various ARM techniques for retrieving liquid and ice cloud microphysical properties, such as water mass content and particle sizes (e.g., Dong and Mace 2003a,b), and biases introduced into them by any filtering must be quantified.

In the following sections we quantify the effects on MMCR data quality that result from the current operational and processing strategies applied to the ARM MMCRs. The analysis includes MMCR data from the ARM sites, the numerical simulation of radar signals, and collocated observations of the NOAA/ETL MMCR and the University of Miami (UM) 94-GHz cloud radar during the National Aeronautics and Space Administration (NASA) Cirrus Regional Study of Tropical Anvils and Cirrus Layers (CRYSTAL)-Florida Area Cirrus Experiment (FACE) experiment that took place in south Florida the summer of 2002. The ETL MMCR has operational settings and sensitivities that are similar to that of the MMCRs deployed at the ARM sites, while the UM cloud radar has a temporal resolution of 2 s and a spatial resolution of 30 m. The comparison provides valuable insights on the effects of ARM MMCR low temporal resolution in terms of cloud representation.

3. Signal and noise characteristics of the ARM MMCRs

Radiatively important clouds, including thin cirrus and boundary layer stratus, often have low reflectivity values that make them difficult to detect with the MMCR, despite the use of different operational modes, because the radar signal returns from clouds are combined with noise in the MMCR receiver. The SNR is often used to express the relative intensities of signals to noise and is given by

$$\mathrm{SNR} = 10 \log\left(\frac{\mathrm{Power}_{\mathrm{signal}}}{\mathrm{Power}_{\mathrm{noise}}}\right). \quad (2)$$

As we will demonstrate, low SNR values are associated with high variance and, hence, potentially large errors in the Doppler moment estimates of radar reflectivity, mean Doppler velocity, and Doppler spectrum width.

Data from the SGP, NSA, and TWP sites were used to evaluate the distribution of observed SNR conditions for stratus, cirrus, and fair-weather cumulus cloud types. The analysis is limited to the boundary layer (mode 1) and cirrus (mode 2) operational modes because they are optimized for the detection of these particular cloud types. Both modes use pulse compression and coherent integration that boost radar sensitivity. Consider time versus height maps of SNR for the different cloud types (Fig. 2). The top rows in Fig. 2 are for stratus and cirrus clouds observed at the ARM NSA site. For the stratus cloud the observing period is 2 days, and during the first 12 h precipitation is observed, as indicated by the streams of high SNR values reaching the ground. The stratus cloud is less than 500 m deep with a cloud base around 200 m above ground level (AGL). At such short ranges pulse compression in mode 1 creates range sidelobes. The cirrus case shows a double-layer structure with prevailing low SNR values. The pair of images in the second row of Fig. 2 shows the same cloud structures as the top row, but after all of the insignificant powers are masked out.

The middle (i.e., third and fourth) rows of panels

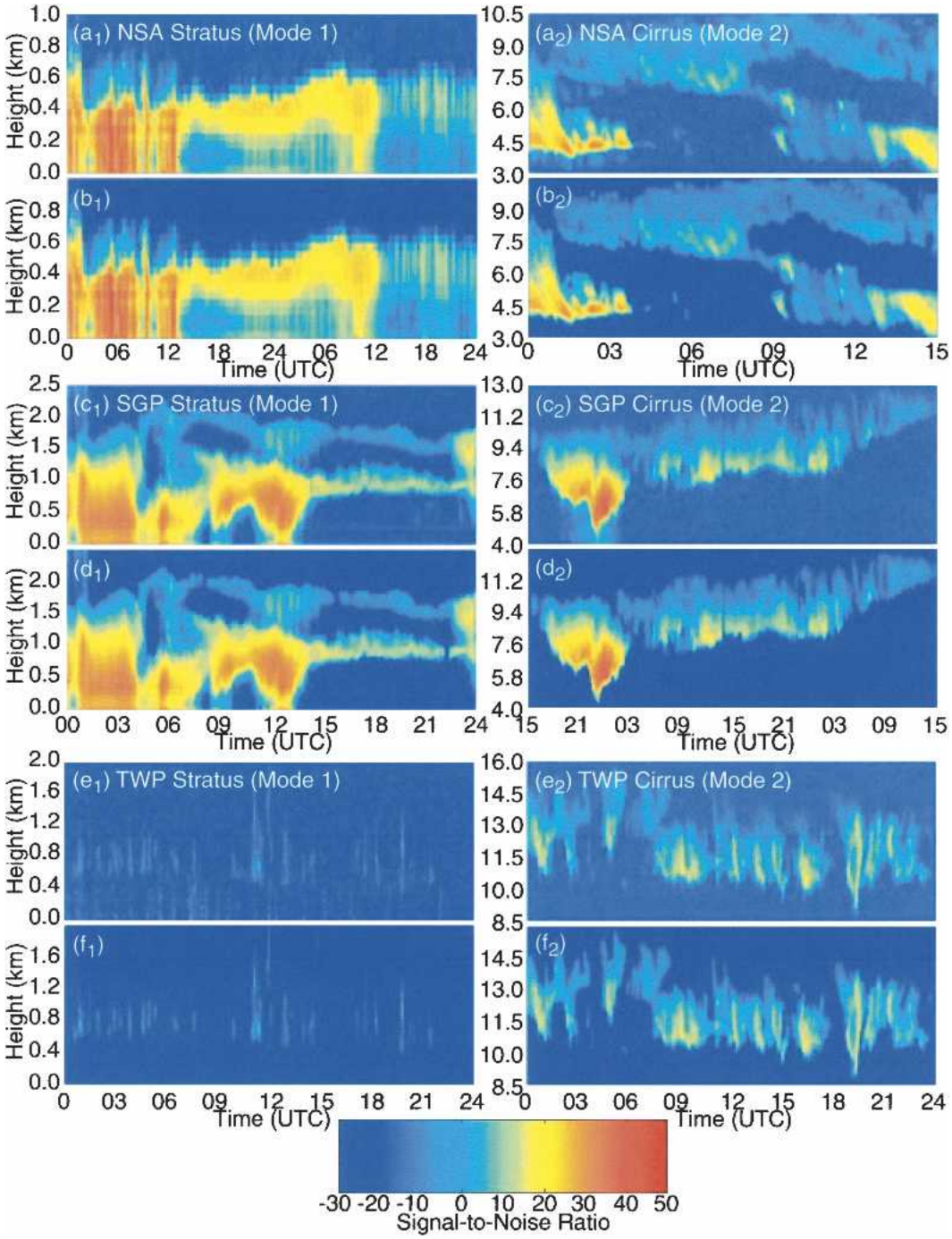

FIG. 2. Examples of SNRs generated by (left) typical boundary layer and (right) cirrus clouds over the (top) NSA, (middle) SGP, and (bottom) TWP ARM sites. For each site and cloud type both the (a), (c), (e) raw and (b), (d), (f) processed radar data are shown. In the analyses of these radar data, the boundary layer mode data are not used for the cirrus cloud studies and the cirrus mode data are not used for the boundary layer cloud studies.

show representative cases of stratus and cirrus clouds at the ARM SGP site. The SGP stratus cloud case is deeper, with a complicated structure and a wide range of SNR values. The stratus cloud case includes both drizzling and nondrizzling periods. The cirrus case is a single cloud layer with low SNR values, especially near the cloud top. Finally, the bottom (i.e., fifth and sixth) rows of panels show examples of broken fair-weather

cumulus and cirrus at the ARM TWP-Nauru site. In the case of the fair-weather cumulus, almost all of the MMCR cloud detections have negative SNR values. This is caused by low radar reflectivities of the fair-weather cumulus. Similarly, the cirrus cloud SNR values are lower compared to the ones observed at both the ARM SGP and NSA sites.

Using the cloud mask of Clothiaux et al. (1995), the insignificant radar powers were removed from the dataset. The in-cloud returns from all four modes were subsequently used to calculate SNR cumulative distributions (CDs) for the cases shown in Fig. 2. In the SNR CDs of Fig. 3 the cirrus mode results for the stratus case and the boundary layer mode results for the cirrus case are excluded. Given the same cloud type and ARM site, the SNR CDs for the different operational modes are similar in shape but are offset along the SNR axis as a result of differences in radar mode sensitivities. For all cloud types at all of the ARM sites, a significant portion of cloud returns are buried in the noise with SNRs less than approximately −10 dB. The SNR values for fair-weather cumulus at the ARM TWP site, in particular, are low. The shift of the SNR CDs to lower SNR values from the boundary layer to general and robust modes for this cloud type (Fig. 3f), with a corresponding drop in the number of significant detections, illustrates the difficulty in detecting these clouds and, thereby, providing a cohesive and continuous cloud mapping between the three modes. The cirrus over the ARM TWP site also exhibits significant portions of returns with negative SNR values.

Overall, the portion of SNR values below −10 dB is significant for all three ARM sites, although high SNR returns from large droplets and ice crystals are also apparent. We use the SNR CDs to develop an understanding of MMCR data quality and to quantify the range of SNR values for each mode and cloud type. In fact, we use SNR values ranging from −20 to 10 dB in our radar simulations for the estimation of errors in the Doppler moment estimates. In addition to SNR characteristics, MMCR receiver noise characteristics, including means and variances, were evaluated. For each range gate j and time step i the MMCR DSP calculates the Doppler spectrum. Note that time i refers to the average of N_{spec} spectra across the signal dwell and processing period. The receiver noise mean power $P_{n,ij}$ appears as a baseline in the Doppler spectrum that must be removed by subtraction before any Doppler spectrum moment is calculated. For the ARM MMCRs, a technique developed by Hildebrand and Sekhon (1974) is used to estimate $P_{n,ij}$. Subsequently, those velocity bins of the Doppler spectrum that are contiguous with the bin containing the peak power and that contain powers above $P_{n,ij}$ are used to estimate the Doppler moments. In the tables and figures of the discussion that follows, $P_{n,ij}$ represents an analog-to-digital (A/D) converter count. The conversion of $P_{n,ij}$ to units of

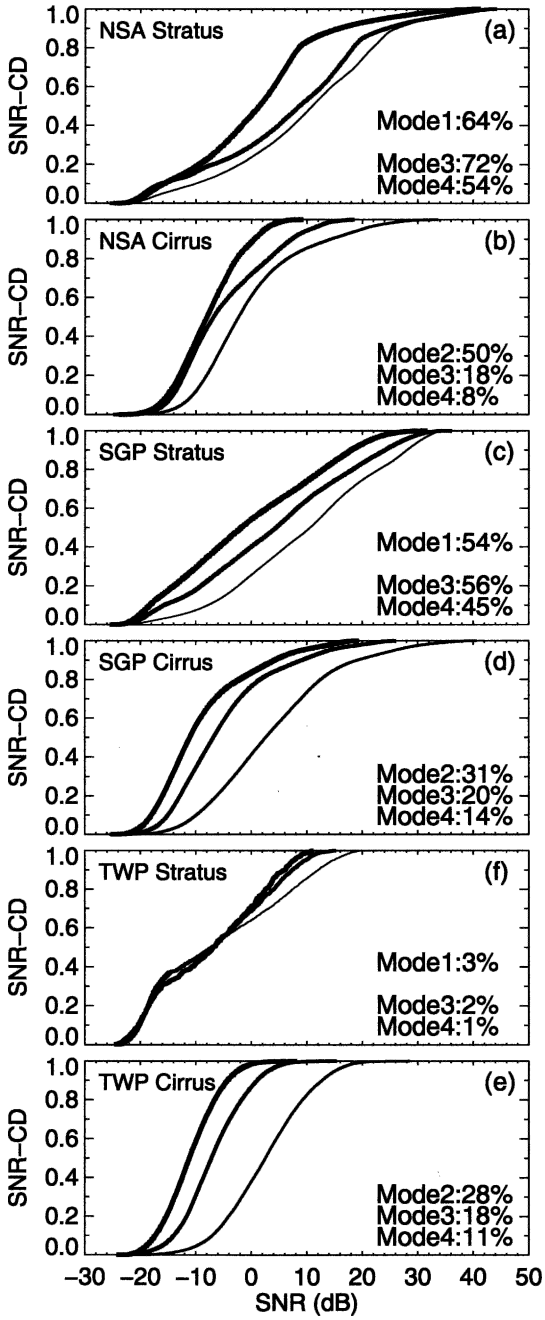

FIG. 3. SNR CDs of the significant cloud radar returns shown in Figs. 2b, 2d, and 2f. The thick lines are for mode 1 or mode 2, depending on cloud type; the medium line is for mode 3; and the thin line is for mode 4. The percentages on the bottom right of each panel were generated by dividing the number of significant detections in Figs. 2b, 2d, and 2f by the (b), (d), (f) total number of range gates present and multiplying the result by 100%.

dBm is 10 $\log_{10}(P_{n,ij})$ minus the MMCR receiver gain (in dB).

Note that $P_{n,ij}$ is computed for each range gate j at the given time step i. Using the receiver noise estimates $P_{n,ij}$ from all N_{gates} range gates at time i, we compute the profile mean noise power $P_{n,i}$ with its associated standard deviation $\sigma_{P_{n,i}}$. We applied this procedure to the mode data from all case study periods at the three ARM program sites. The resulting histograms of $P_{n,i}$ and $\sigma_{P_{n,i}}$ are presented in Fig. 4. Narrow distributions of $P_{n,i}$ are indicative of a stable MMCR receiver, while fluctuations in $P_{n,i}$ affect radar sensitivity by reducing the SNR (e.g., Gordon 1997). These variations are often the result of changes in the environmental (e.g., temperature and humidity) conditions of the MMCR receiver. Highly variable noise floor estimates along the radar range can also be attributed to hardware, low SNR conditions, or wide Doppler spectra. As Fig. 4 illustrates, the ARM NSA MMCR receiver noise mean powers $P_{n,i}$ exhibit the best characteristics, because the noise mean power distributions are narrow, implying stable noise for the four modes across all of the case study periods. At the other two sites, especially the ARM TWP-Nauru site, the characteristics of the MMCR receiver noise mean powers $P_{n,i}$ exhibit higher variability.

In addition to the distribution of the noise mean powers $P_{n,i}$, the distribution of the standard deviations $\sigma_{P_{n,i}}$ of the noise powers $P_{n,ij}$ is also shown. High values of $\sigma_{P_{n,i}}$ are indicative of highly variable noise mean powers. When the MMCR receiver is operationally stable, the distribution of $\sigma_{P_{n,i}}$ is narrow, with a 0.2-dB total width, as for the ARM NSA cirrus case. However, several cases at the ARM SGP and TWP sites have wide 0.2–2.0-dB distributions of $\sigma_{P_{n,i}}$. Overall, there is a significant correlation between $P_{n,i}$ and $\sigma_{P_{n,i}}$. Comparing the SNR CDs and the histograms of receiver noise characteristics, we conclude that wide $\sigma_{P_{n,i}}$ distributions are correlated with low SNR values. The effect of signal characteristics, including SNR and Doppler spectrum width, on the noise mean power estimates is analyzed in the following section.

Time versus height mappings of the MMCR receiver noise power estimates $P_{n,ij}$ during the ARM SGP stratus case study period for all four modes is shown in Fig. 5. Enhancements of the receiver noise power estimates are observed throughout the mappings, which are magnified in the boundary layer mode (mode 1) and minimized in the robust mode (mode 4). The yellow vertical streaks (and some of the weaker streaks) in Fig. 5 are a result of enhanced emission from the large liquid water path above the radar. The time–height locations of mode-1-enhanced receiver noise estimates resemble the cloud structure, as a comparison of Fig. 5a to Fig. $2d_1$ illustrates. A significant number of boundary layer mode radar range gates exhibit an enhancement of the receiver noise powers $P_{n,ij}$ during periods of large cloud reflectivities in the boundary layer. One example is the 0–6-h time period of drizzling stratus at the ARM SGP site. While such an effect might equally affect all MMCR modes, mode 4 is actually the least impacted, because this mode has no coherent integration and a wide Nyquist velocity interval. During drizzling conditions, the Doppler spectrum occupies a significant portion of the Doppler velocity range in all modes with coherent integration. In such cases, estimation of the Doppler spectra noise powers is questionable and biases are introduced. In the following section the limitations of the Hildebrand and Sekhon (1974) Doppler spectrum noise estimation technique are investigated, especially under wide Doppler spectrum conditions.

The number of radar pulses N_{pulses} contributing to a set of Doppler moment estimates and the signal bandwidth, as measured by the Doppler spectrum width σ_w, are additional factors that influence the variance of the Doppler moment estimates. White noise samples are independent and the integration of N_{pulses} noise samples results in a decrease of the variance in the noise mean power estimates by a factor of N_{pulses}. Radar signals are narrowband and, thus the number of independent samples $N_{\text{pulses,in}}$ is smaller than N_{pulses}. In fact, the number of independent samples $N_{\text{pulses,in}}$ is a function of the total number of radar samples integrated N_{pulses} and the Doppler spectrum width σ_w (e.g., Doviak and Zrnić 1993). For narrow Doppler spectrum widths the correlation of the samples is high, and the application of coherent integration to the radar signal samples improves the SNR and reduces the variance of the Doppler estimates. As the Doppler spectrum width σ_w increases, the correlation between the radar signal samples decreases and coherent integration is less effective, especially if the signal occupies a large portion of the Nyquist velocity interval Table 1. The number N_{pulses} of radar samples for the current operational modes is shown.

4. Doppler radar signal simulation

Doppler radar signal simulation has been extensively used in the past as a method to evaluate the performance of Doppler moment estimators (e.g., Zrnic 1979; Sirmans and Bumgarner 1975; May and Strauch 1989) and theoretical calculations of performance curves abound in the literature (e.g., Doviak and Zrnić 1993; Frehlich and Yadlowsky 1994). The ARM MMCRs implement several different operational modes

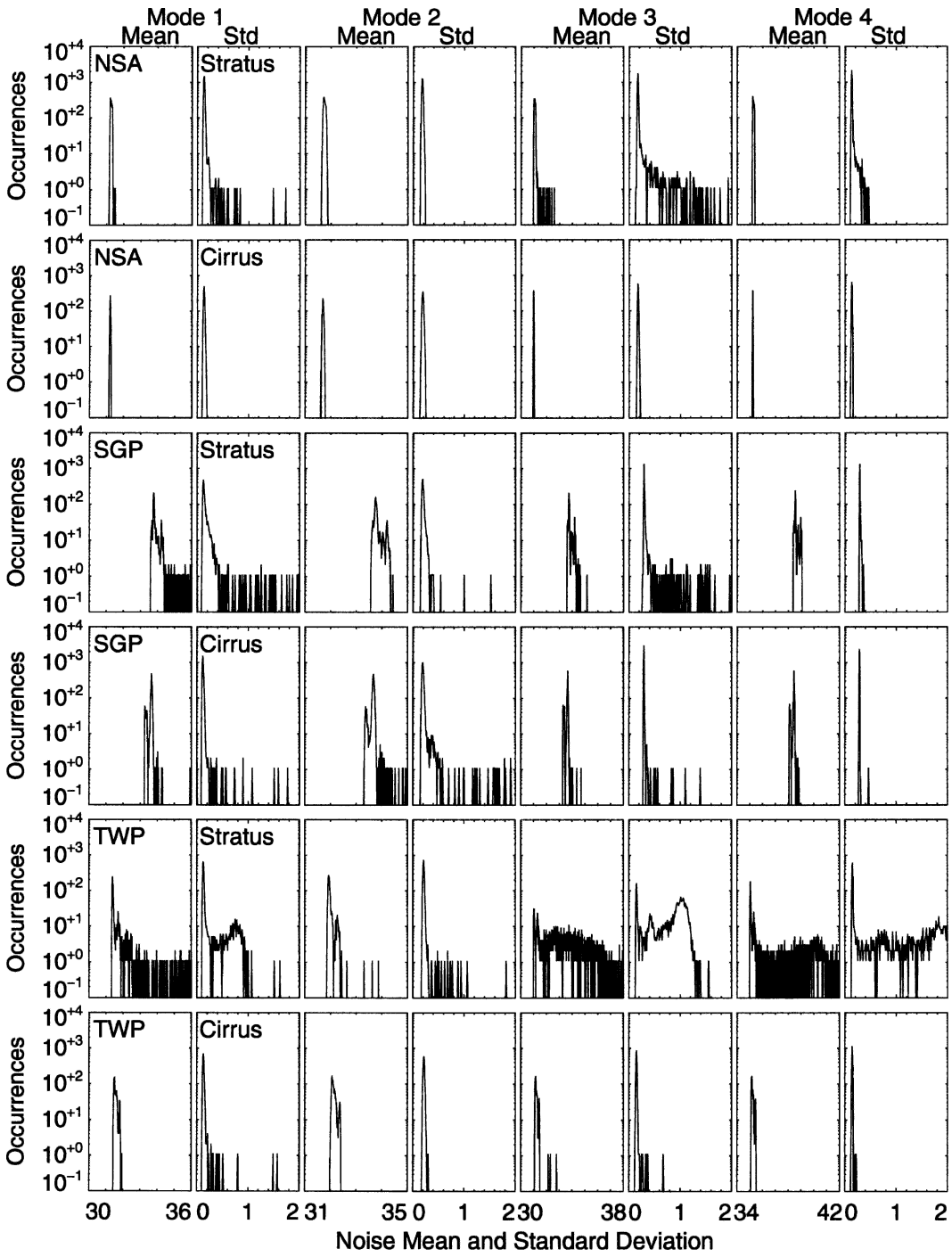

FIG. 4. Frequency of occurrence histograms of MMCR receiver noise mean powers and standard deviations for all three ARM sites and all four operational modes. The healthy radar receivers are characterized by narrow distributions of receiver mean noise powers and small values for the receiver mean noise power standard deviations. The mean noise powers are presented as $10 \log_{10}(P_{n,i})$, while the mean noise power standard deviations are presented as $10 \log_{10}([P_{n,i} + \sigma_{P_{n,i}}]/P_{n,i})$.

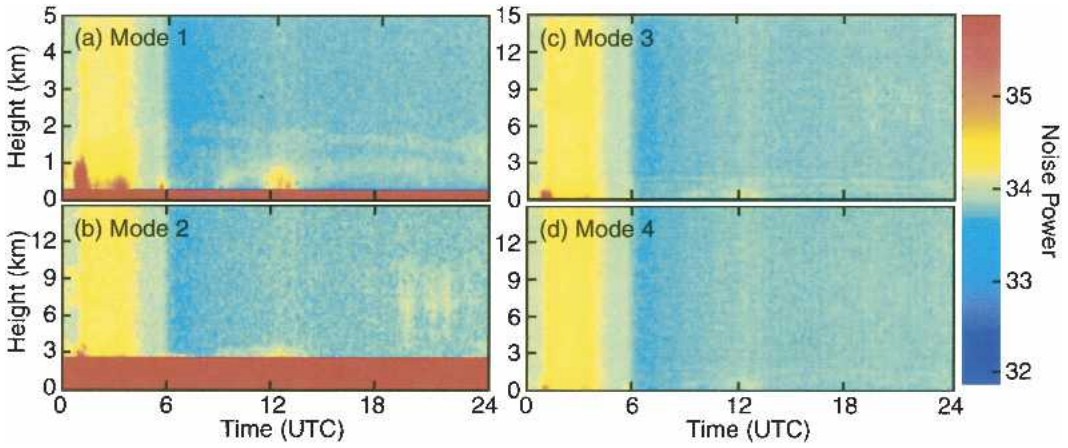

FIG. 5. Time vs height mappings for all four modes of MMCR receiver noise power estimates during the ARM SGP site stratus case study period. The noise powers are presented as 10 $\log_{10}(P_{n,ij})$.

(Clothiaux et al. 1999) and coherent integration of the in-phase (i.e., I_t) and quadrature-phase (i.e., Q_t) radar signal voltage time series. Numerical simulations of the I_t and Q_t radar signals allow us to evaluate the performance of the MMCR Doppler moment estimators under controlled conditions and for any set of operational parameters.

The output of the MMCR receiver is composed of a complex voltage signal S_t given by

$$S_t = I_t + jQ_t, \tag{3}$$

where I_t and Q_t are the in-phase and quadrature-phase components of the complex radar signal produced by the demodulators. Zrnic (1975) proposed a simulation method for Doppler spectra and signals. According to this method, time series of I_t and Q_t can be generated by the discrete inverse Fourier transform of white noise multiplied by a filter with the desired Doppler spectrum shape. Because the radar signals at the port of the receiver have an average strength and probability distribution that depends on the atmospheric scatterers, Lhermitte and Kollias (1999) simulated the I_t and Q_t voltage pairs with equations that explicitly treated each particle,

$$I_a(k) = \sum_{i=1}^{N_{\text{scat}}} A_i \cos\{2\pi([\omega_o + \sigma_o g(i)]k + \phi(i))\} \tag{4a}$$

and

$$Q_a(k) = \sum_{i=1}^{N_{\text{scat}}} A_i \sin\{2\pi([\omega_o + \sigma_o g(i)]k + \phi(i))\}, \tag{4b}$$

where N_{scat} represents the number of individual scatterers (i.e., hydrometeors) within the radar resolution volume that contribute to the radar signal, A_i is the amplitude that results from each scatterer, and $g(i)$ and $\phi(i)$ are random values drawn from Gaussian and uniform distributions, respectively. In the equations, the characteristics of the cloud signals have been treated as narrowband Gaussian signals with central frequency ω_o and standard deviation σ_o. The random values $\phi(i)$ drawn from the uniform distribution represent the initial phases that result from the random locations of the cloud particles. The subscript a indicates the atmospheric contribution to the radar signal. The number N_{scat} of scatterers should be as large as possible in order to produce reliable statistics; in our simulations we set N_{scat} to 32 768.

In the receiver circuits I_a and Q_a are combined with receiver noise that has its own strength and probability distribution. The noise fluctuations add random components I_n and Q_n to the atmospheric components I_a and Q_a and are calculated according to the following equations:

$$I_n(k) = N(k)\cos[2\pi\psi(k)] \tag{5a}$$

and

$$Q_n(k) = N(k)\sin[2\pi\psi(k)], \tag{5b}$$

where $N(k)$ is the Gaussian-distributed noise amplitude and $\psi(k)$ is a uniformly distributed random phase. The radar signals I_t and Q_t at the output of the MMCR receiver are given by

$$I_t = CI_a + I_n \tag{6a}$$

and

$$Q_t = CQ_a + Q_n, \tag{6b}$$

where the coefficient C depends on the relative strength of the atmospheric signal and receiver noise, which is often quantified by the SNR, given as

$$\mathrm{SNR} = 10 \log \left(\frac{\sum_{k=1}^{k=N_{\mathrm{pulses}}} \sqrt{[I_a^2(k) + Q_a^2(k)]}}{\sum_{k=1}^{k=N_{\mathrm{pulses}}} \sqrt{[I_n^2(k) + Q_n^2(k)]}} \right), \quad (7)$$

where N_{pulses} is the number of simulated I_t and Q_t samples.

We used the simulated I_t and Q_t signals to evaluate the performance of the Doppler moment estimates obtained by the MMCRs. For a specified set of values for SNR, ω_o, and σ_{o}, we simulated a large number of I_t and Q_t samples and processed them with the MMCR DSP algorithms. The MMCR DSPs apply FFT processing to the I_t and Q_t time series. If time domain, that is, coherent, averaging is applied prior to FFT processing, the length of the original I_t and Q_t time series is reduced by a factor of N_{ci}, where N_{ci} is the number of coherent integrations. Coherently integrated radar signals $I_{t,\mathrm{ci}}$ and $Q_{t,\mathrm{ci}}$ are given by

$$I_{t,\mathrm{ci}}(k) = \sum_{i=(k-1)N_{\mathrm{ci}}+1}^{kN_{\mathrm{ci}}} I_{\mathrm{t}}(i)\mathrm{BH}\{i - [(k-1)N_{\mathrm{ci}}]\} \quad (8a)$$

and

$$Q_{t,\mathrm{ci}}(k) = \sum_{i=(k-1)N_{\mathrm{ci}}+1}^{kN_{\mathrm{ci}}} Q_{\mathrm{t}}(i)\mathrm{BH}\{i - [(k-1)N_{\mathrm{ci}}]\}, \quad (8b)$$

where BH represents the Blackman–Harris filter coefficients.

5. Standard deviation of MMCR Doppler moments

The Doppler power density spectrum $S(v) = dZ/dv$ [in units of $\mathrm{mm}^6\ \mathrm{m}^{-3}\ (\mathrm{m\ s}^{-1})^{-1}$] is often recorded after FFT processing of the radar I/Q signals. Once $S(v)$ is estimated from the $I_t + jQ_t$ time series, the noise mean power estimate is removed by subtraction and the moments are estimated from that part of the Doppler spectrum occupied by the atmospheric signal. While there are many different methods for Doppler spectrum noise estimation, MMCR processing uses a technique developed by Hildebrand and Sekhon (1974). Although the full Doppler spectrum $S(v)$ is needed to capture the full radial velocity statistics of the targets and to identify spurious frequency components, the Doppler moments comprise a substantial part of the information that is necessary for assessment of the microphysical and dynamical properties in clouds.

The performance of the FFT Doppler moment estimator was evaluated for SNR values ranging from −20 to 20 dB, normalized mean Doppler velocities w_n from 0.00 to 0.05, and normalized Doppler spectrum widths σ_n from 0.0 to 0.1, where normalization is with respect to the full-scale Nyquist velocity. That is, we normalize the mean Doppler velocities w and Doppler spectrum widths σ_w by twice the Nyquist velocity, that is, $2V_{\mathrm{ny}}$, to produce the normalized mean Doppler velocities w_n and Doppler spectrum widths σ_n. In the simulations we set N_{pulses} to 8192 pairs of I/Q radar signals. After simulating a time series of N_{pulses} I/Q radar signal pairs for a set of SNR, w_n, and σ_n parameter values, we adopted two different processing paths for the I/Q radar signals. For the first signal processing methodology we applied coherent integration with N_{ci} set to 8, reducing the length of the I/Q time series to $N_{\mathrm{pulses}}/N_{\mathrm{ci}}$, or 1024. Afterward, 64-point FFTs were computed and the resulting 16 Doppler power density spectra were averaged. (Note that $N_{\mathrm{fft}} = 64$ and $N_{\mathrm{spec}} = 16$.) In this path the Nyquist velocity V_{ny} equals $0.5/N_{\mathrm{ci}}$. In the second signal processing path no coherent integration is applied (i.e., $N_{\mathrm{ci}} = 1$), and the original N_{pulses} I/Q radar signal time series was used to obtain sixteen 512-point FFTs. (That is, N_{fft} and N_{spec} are now 512 and 16, respectively.) We then averaged the 16 Doppler power density spectra to arrive at our final spectrum with a Nyquist velocity V_{ny} of 0.5. Using the two signal processing paths, with and without coherent integration, we evaluated the advantages and disadvantages of using coherent integration for a variety of cloud and, hence, signal, conditions. For each set of input parameters (i.e., set of SNR, w_n, and σ_n values), 50 I/Q time series were simulated and the Doppler moments were calculated for each signal processing method.

a. Errors due to SNR and signal bandwidth

The standard deviations of the Doppler moment estimates derived from the numerical simulations are illustrated in Fig. 6. The abscissa Φ ($= N_{\mathrm{pulses}} 10^{\mathrm{SNR}/10}$) is the product of the simulated SNR and the number N_{pulses} of radar signal I/Q samples (e.g., Frehlich and Yadlowsky 1994; Lottman and Frehlich 1997). Plotting the standard deviations versus the parameter Φ generalizes the results for all four modes with different N_{pulses} and SNR. For example, mode 1 at the SGP site uses 40 000 radar samples for each Doppler moment estimate. If the SNR is −10 dB, the standard deviation of the Doppler moment estimates can be found at the abscissa value of 4000 in Fig. 6, which is also the standard deviation for a variety of other combinations of N_{pulses} and SNR.

The top row of Fig. 6 shows the standard deviation of

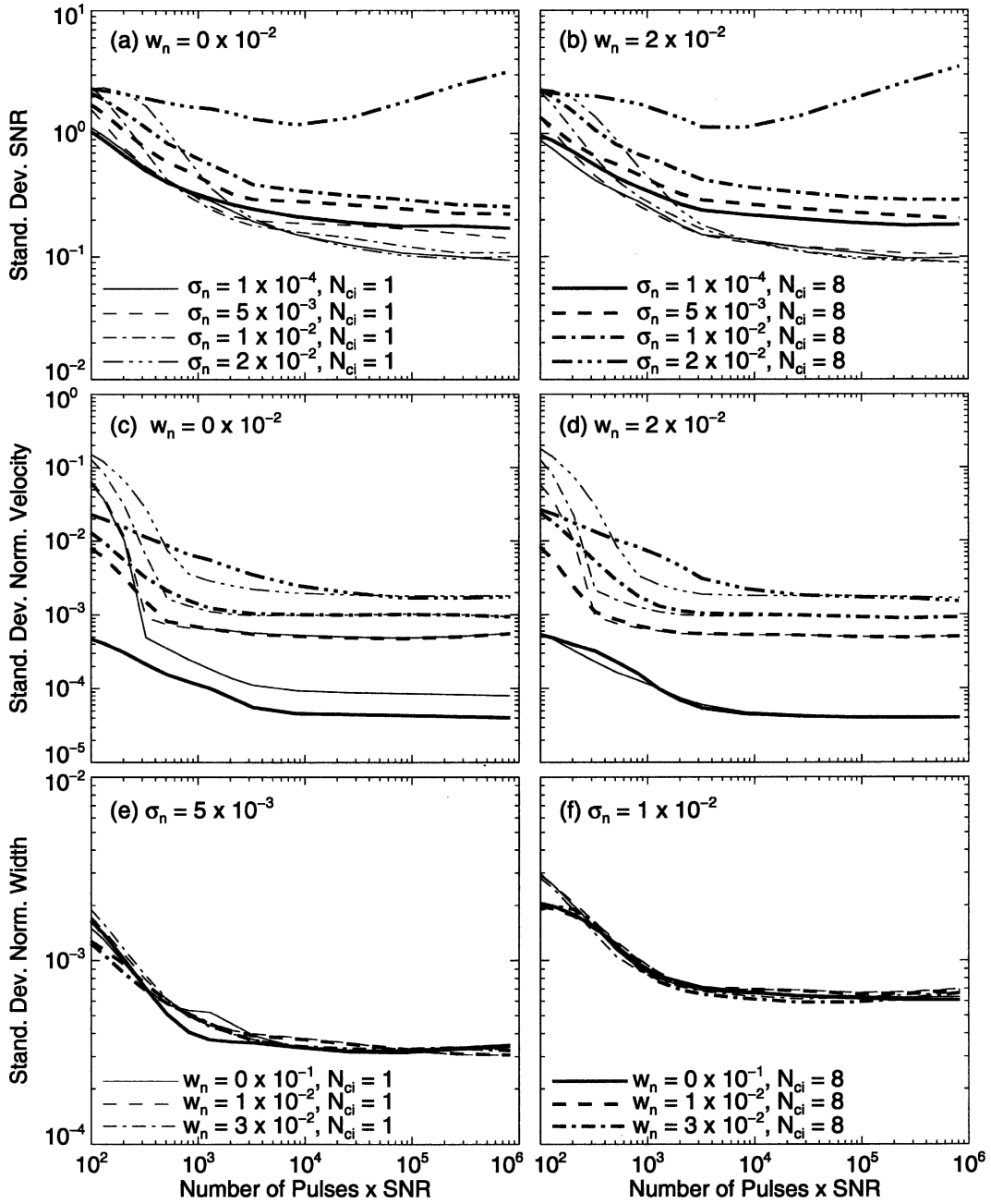

FIG. 6. (top) Standard deviations of the SNR estimates vs Φ for a range of Doppler spectrum width values σ_n and two mean Doppler velocities w_n of (a) 0 and (b) 2×10^{-2}. (middle) Standard deviations of the mean Doppler velocity estimates vs Φ for a range of Doppler spectrum width values σ_n and two mean Doppler velocities w_n of (c) 0 and (d) 2×10^{-2}. (bottom) Standard deviation of the Doppler spectrum width estimates vs Φ for a range of mean Doppler velocities w_n and two Doppler spectrum width values σ_n of (e) 5×10^{-3} and (f) 1×10^{-2}. Thick lines represent results with N_{ci} set to 8 and thin lines correspond to results with N_{ci} set to 1. The legends in (a) and (b) apply to (a)–(d), while the legends in (e) and (f) apply to (e)–(f).

the SNR estimates for Doppler spectrum width values σ_n of 1×10^{-4}, 5×10^{-3}, 1×10^{-2}, and 2×10^{-2} and mean Doppler velocities w_n of 0.0 (Fig. 6a) and 0.02 (Fig. 6b). The thick lines represent results with N_{ci} set to 8 and thin lines correspond to results with N_{ci} set to 1. Naturally, as the parameter Φ decreases because of lower SNR or a smaller number of samples N_{pulses}, the standard deviation of the SNR estimates increases. For

values of Φ above 10^4 the influence of the receiver noise power is negligible and the spread of the SNR estimates depends only on the Doppler spectrum width, which also determines the number of independent samples $N_{\text{pulses,in}}$ and, thus, the signal variance reduction. At small Φ values, less than 10^3, the receiver noise characteristics strongly influence the spread of the SNR estimates and small changes in the parameter Φ result in large changes in the estimate of the SNR standard deviation. Overall, avoiding estimation of Doppler moments at Φ values below 300 is desirable; otherwise, the resulting Doppler moment estimates have large uncertainties. According to the MMCR receiver transfer function, that is, SNR versus radar reflectivity, a standard deviation of 1 dB in the SNR estimate at low SNR conditions is equivalent to a 6-dB error in the cloud reflectivity estimate Z_e (in units of dBZ_e). At higher SNR values, the receiver transfer function is linear and less sensitive to the spread of the SNR estimates.

Coherent integration works best for narrow Doppler spectrum widths of less than 10^{-4} and near-zero mean Doppler velocities. For typical cloud spectrum width values (i.e., $\sigma_n \approx 10^{-2}$) the standard deviation of the SNR estimates with coherent integration are equivalent to those without coherent integration only for Φ less than approximately 200. At large Φ values, the spread in the SNR estimates is higher when coherent integration is implemented because the noise is not a factor and coherent integration actually reduces the number of independent samples. The worst estimates are produced by coherent integration of wideband Doppler spectrum width signals.

The middle row of Fig. 6 shows the standard deviation of the mean Doppler velocity estimates for Doppler spectrum width values σ_n of 1×10^{-4}, 5×10^{-3}, 1×10^{-2}, and 2×10^{-2} and mean Doppler velocities w_n of 0.0 (Fig. 6c) and 0.03 (Fig. 6d). Consider the results for the typical cloud spectrum width value of 2×10^{-2}. For Φ equal to 100, the standard deviation of the mean Doppler velocity is approximately (10^{-2}) $(2V_{\text{ny}})$ for the coherently integrated signal processing path and (10^{-1}) $(2V_{\text{ny}})$ with no coherent integration. Beyond Φ of 10^4, the spread in the mean Doppler velocity estimates converges for both signal processing paths. The numerical simulation illustrates the superior performance of coherent integration at low Φ values, especially for narrow Doppler spectrum width values. For the numerical simulations velocity aliasing was not explicitly considered, with only partial Doppler velocity aliasing produced in the cases of wide Doppler spectrum widths and a mean Doppler velocity different from zero. The effect of coherent integration on mean Doppler velocity estimates when velocity aliasing is present is investigated in the following section.

The bottom row of Fig. 6 shows the performance of the Doppler spectrum width estimates for the two signal processing paths. The results for two input Doppler spectrum width values σ_n of 5×10^{-3} (left panel) and 1×10^{-2} (right panel) are shown for mean Doppler velocity values w_n of 0, 1×10^{-2}, and 3×10^{-2}. The spread in the Doppler spectrum widths σ_n converge quickly and for the worst sampling conditions, that is, low Φ values, the standard deviation is on the order of (2×10^{-3}) $(2V_{\text{ny}})$.

b. *Errors and fluctuations in noise mean power estimates*

The MMCR receiver noise is generated inside the mixers and amplifiers. The noise power and its variance are central to the determination of SNR and radar sensitivity. For example, small changes in the receiver noise characteristics can affect significantly the MMCR cloud reflectivity estimates, especially at low SNR conditions. At low SNR values a 1-dB change in the SNR estimate results in a 6-dB change in the cloud reflectivity estimate. Thus, for SNR values less than approximately -10 dB, accurate measurements of receiver noise are critical. Analysis of the ARM MMCR receiver noise characteristics revealed several interesting features. While jumps in the noise mean power, as well as highly variable noise estimates for gates across a vertical profile, can be attributed to hardware performance, elevation of the noise mean power estimates for range gates where strong echoes are observed (e.g., Fig. 5) is associated with atmospheric signal return and signal processing.

The correlations between the estimated mean noise power and the signal SNR and Doppler spectrum width σ_n for the boundary layer and robust modes are illustrated in Fig. 7 for the SGP stratus case (Fig. $2c_1$). In the top two rows of Fig. 7 scatterplots of receiver noise mean power $P_{n,ij}$ as a function of SNR and Doppler spectrum width σ_n are shown for mode 1. As the figure illustrates, for values of SNR and σ_n that approach and exceed 20 dB and 0.6 m s^{-1}, respectively, the Hildebrand and Sekhon (1974)-estimated noise mean powers increase by as much as 5–6 dB. Note that mode 1 is the boundary layer mode and uses coherent integration that reduces the Nyquist velocity to 3 m s^{-1}. For spectrum widths more than 0.6 m s^{-1} (i.e., $\sigma_n > 0.1$) the Doppler power density spectrum occupies a significant fraction of the Doppler spectrum. Under such conditions, the noise mean power estimates are biased high, leading to significant errors in the Doppler moment estimates.

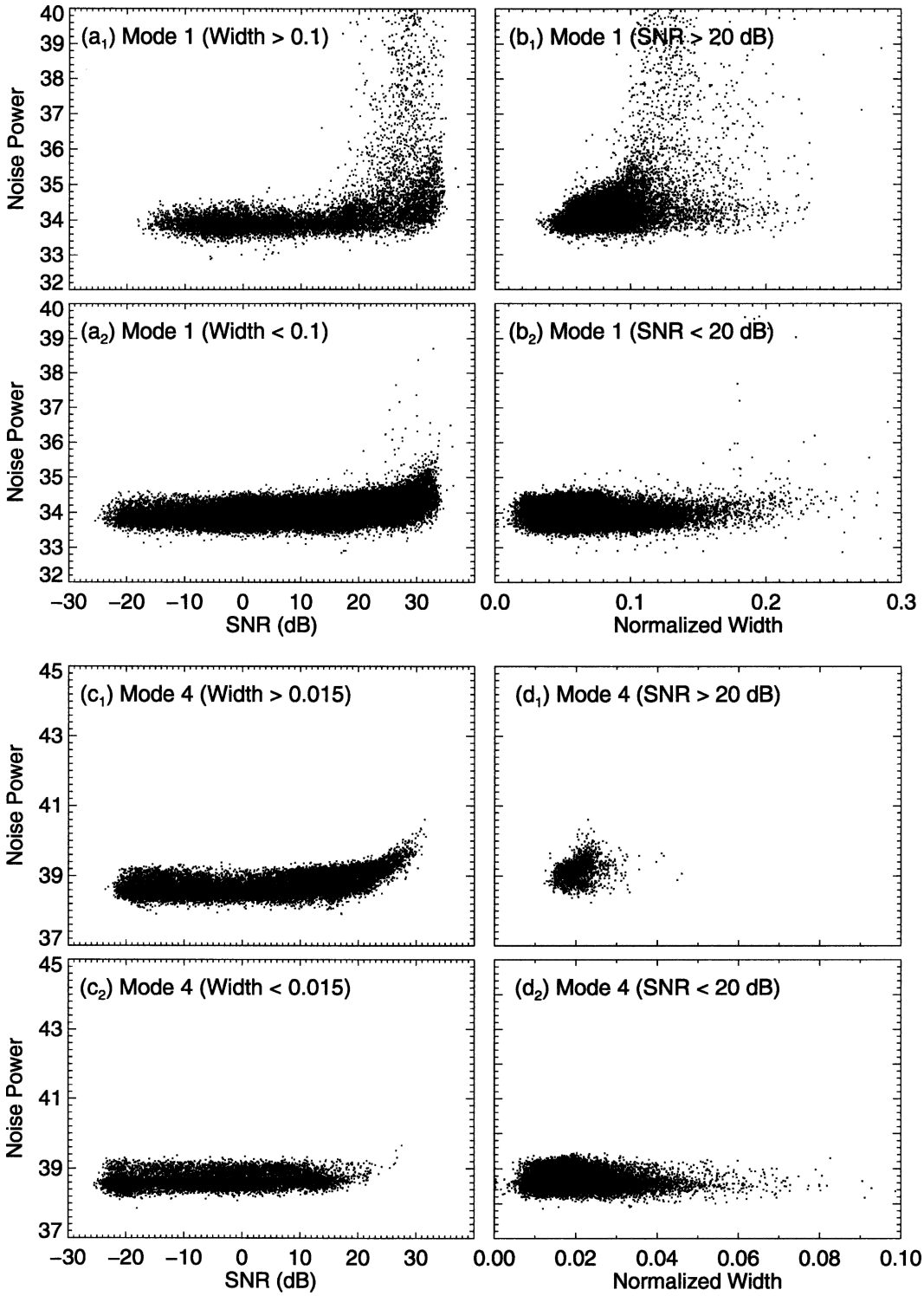

FIG. 7. Noise power estimates [presented as 10 $\log_{10}(P_{n,ij})$] vs (left) SNR and (right) normalized Doppler spectrum width for the (top) boundary layer and (bottom) robust modes. The noise power vs SNR plots are segregated into low and high Doppler spectrum width sample populations, while the noise power vs normalized Doppler spectrum width plots are segregated into low and high SNR sample populations.

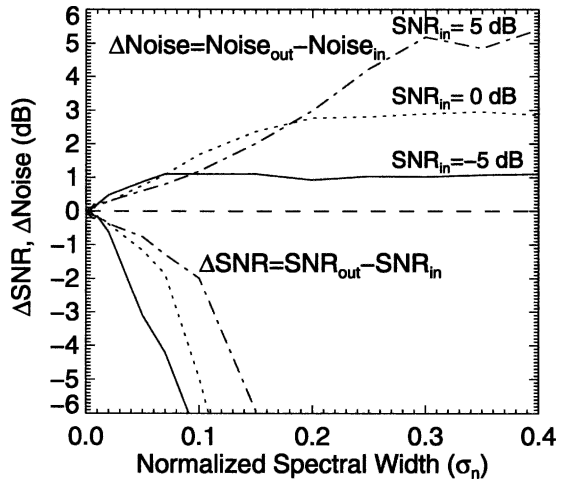

FIG. 8. Results of numerical simulations of the performance of the Hildebrand and Sekhon (1974) Doppler spectrum noise estimator technique for a range of Doppler spectrum widths. For larger normalized Doppler spectrum widths errors in the noise power estimates occur, leading to a decrease in SNR.

The analysis of mode 4 (bottom two rows of Fig. 7) provides additional support for our conclusions. Recall that mode 4 has no coherent integration and its Nyquist velocity interval is ± 20 m s^{-1}. The part of the Doppler spectrum that is occupied by the signal returns is a small portion of $2V_{ny}$, and mode 4 data scatterplots do not exhibit correlations between the signal characteristics and receiver noise mean power estimates. The small, approximately 1 dB, increase of the Doppler spectrum noise mean power for large SNR values most likely results from atmospheric emission.

Using numerical simulations of I/Q radar signals for a set of SNR and σ_n values, we found that the Hildebrand and Sekhon (1974) technique overestimates the receiver noise mean power $P_{n,i}$ as σ_n increases, asymptotically approaching an upper bound that depends on SNR (Fig. 8). For example, for an SNR of 0 dB the asymptotic value is 3 dB; that is, the noise mean power estimate is twice its actual value and the entire signal is taken to be part of the noise. The overestimation in the receiver noise mean power as a result of the limitations of the Hildebrand and Sekhon (1974) technique, in turn, influences estimation of SNR (Fig. 7) and, hence, the cloud reflectivity. Hildebrand and Sekhon (1974) address the limitation of their thresholding technique in their paper. They wrote "When the bound-to-bound width of the Doppler spectrum approaches one-half of the unambiguous frequency span, the Doppler spectrum begins to lose much of its ability to make meaningful measurements. In such a case, the technique described for determining the noise threshold appears to work well in spite of the large width of the spectrum. With wider spectra, the thresholding technique would begin to produce erroneous results." The bias in the cloud reflectivity is significant, suggesting that widening of the Doppler spectrum Nyquist velocity V_{ny} for the MMCR operational modes by decreasing N_{ci} will improve the accuracy of the Doppler moment estimates. While results for modes 1 and 4 are illustrated in Fig. 8, modes 2 and 3, which also include coherent integration, exhibit similar receiver noise behavior.

A comprehensive analysis of MMCR data from the SGP, NSA, and TWP ARM sites was conducted to evaluate the behavior of the spectra noise floors under high radar reflectivity and spectrum width conditions. A month of MMCR data from each ARM site was analyzed to study the fluctuation of the receiver noise mean power calculated from the MMCR Doppler spectra using the Hildebrand and Sekhon (1974) spectral noise estimation technique. At each ARM site, and for each mode, a receiver noise mean power value was estimated for low ($Z \leq -10$ dBZ) and high ($Z > -10$ dBZ) reflectivity estimates (Table 2) and low ($\sigma_n \leq 0.1$) and high ($\sigma_n > 0.1$) Doppler spectrum width values (Table 3). The results are consistent with the analysis of the observations (Fig. 7) and the numerical simulations (Fig. 8). As Table 2 illustrates, all modes with short Nyquist boundaries exhibit significant jumps in the estimated spectral noise floors from the population of

TABLE 2. Receiver noise power averages for populations of low and high radar reflectivity values for each operational mode of the MMCRs at each of the three ARM program sites. The units of Z are dBZ in the table header. The average noise powers are reported as 10 times the logarithm to the base 10 of averages of the relevant A/D converter counts returned by the Hildebrand and Sekhon (1974) Doppler spectrum noise power estimation algorithm.

	SGP		TWP		NSA	
Mode	$Z \leq -10$	$Z > -10$	$Z \leq -10$	$Z > -10$	$Z \leq -10$	$Z > -10$
Boundary layer	28.8	40.2	31.9	42.9	35.2	37.3
Cirrus	29.5	46.5	32.9	46.4	37.1	47.1
General	28.5	32.9	31.6	36.9	34.5	33.9
Robust	33.5	34.5	36.4	36.9	38.8	38.8

TABLE 3. Receiver noise power averages for populations of low and high Doppler spectrum width values for each operational mode of the MMCRs at each of the three ARM program sites. The Doppler spectrum width values are normalized and dimensionless. The average noise powers are reported as 10 times the logarithm to the base 10 of averages of the relevant A/D converter counts returned by the Hildebrand and Sekhon (1974) Doppler spectrum noise power estimation algorithm.

	SGP		TWP		NSA	
Mode	$\sigma_n \leq 0.1$	$\sigma_n > 0.1$	$\sigma_n \leq 0.1$	$\sigma_n > 0.1$	$\sigma_n \leq 0.1$	$\sigma_n > 0.1$
Boundary layer	28.6	34.1	31.6	36.9	35.2	36.0
Cirrus	29.9	38.7	32.6	39.4	37.0	39.9
General	28.5	30.7	31.4	33.8	34.5	34.4
Robust	33.4	36.5	36.3	37.0	38.8	38.7

small to high reflectivities. The robust mode with wide Nyquist velocity boundaries shows no, or little, dependence of the estimated spectra noise floor on reflectivity. Similar behavior is documented for low and high Doppler spectrum width values (Table 3). Note that high values of Doppler spectrum width are more frequently observed at the SGP and TWP sites and less at the NSA site, while the number of samples of high Doppler spectrum width values for the robust mode is small because of its wide Nyquist velocity boundaries.

c. Coherent integration gain evaluation

Coherent integration of the I_t and Q_t time series was described in section 4 and is popular in VHF and UHF radar systems (e.g., Schmidt et al. 1979). The use of coherent integration has a twofold objective. By coherently integrating the I_t and Q_t radar signal pairs from N_{ci} consecutive radar pulses before digitization, the amount of data for processing is reduced. While, 20 yr ago, data reduction was a critical issue because of the limited sampling capability of A/D converters, A/D converters today have sampling capabilities of several megasamples per second. Besides data reduction, coherent integration offers SNR improvements. Under optimum conditions of narrow Doppler spectrum widths σ_n and zero-mean Doppler velocities w_n, the improvement is proportional to a factor of N_{ci}. However, coherent integration decreases the Doppler spectrum Nyquist velocity V_{ny} by a factor of N_{ci}. As SNR improvements from coherent integration are a result of bandwidth noise reduction while maintaining the signal bandwidth comfortably within the reduced Nyquist velocity interval $2V_{ny}/N_{ci}$, any improvements in SNR resulting from a coherent integration decrease if the mean Doppler velocity tends toward one of the reduced Nyquist velocities $\pm V_{ny}/N_{ci}$ or the Doppler spectrum width σ_n approaches a significant fraction of $2V_{ny}/N_{ci}$.

To illustrate SNR improvements that result from coherent integration with N_{ci} equal to 8 consider Fig. 9. Numerical simulations of I/Q radar signals were used to evaluate the performance of coherent integration for a set of Doppler spectrum widths σ_n of 1×10^{-3}, 5×10^{-3}, and 1×10^{-2}, and for mean Doppler velocities shifted away from zero. As the mean Doppler velocity moves away from zero, the coherent integration gain, with a maximum of 9 dB, decreases. As the signal bandwidth (i.e., σ_n) increases, the radar signal samples become more independent and coherent integration again leads to a degradation in SNR. For small σ_n the simulated gain from coherent integration matched theoretical predictions that were based on extremely narrow spectrum widths until the mean Doppler velocity approached the reduced Nyquist velocity of 0.0625. As the Doppler spectrum width increased, deviations from theoretically calculated gains were larger and occurred well before the reduced Nyquist velocity. We conclude

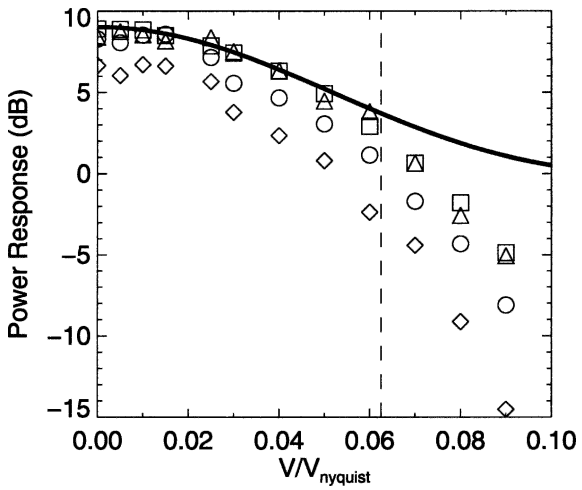

FIG. 9. Evaluation of the coherent integration gain for Doppler spectrum width σ_n values of 1×10^{-4} (squares), 5×10^{-3} (triangles), 1×10^{-2} (circles), and 2×10^{-2} (diamonds) and a wide range of mean Doppler velocities using numerical simulations. The solid line shows the theoretically estimated gain as a function of the mean Doppler velocity for extremely narrow Doppler spectrum widths. The vertical dashed line indicates the position of the reduced Nyquist velocity.

that for σ_n exceeding a value of 0.1, coherent integration should not be implemented.

Currently, no correction is applied to ARM MMCR signal processing to account for deviations of SNR gains from expected theoretical estimates that result from coherent integration of wideband radar Doppler spectra with potentially nonzero mean Doppler velocities. Because of their long wavelength and high PRF, VHF and UHF radar profilers have large Nyquist velocities V_{ny}, as well as signals that occupy only a small portion of the Doppler spectrum close to zero Doppler velocities. Hence, coherent integration is quite effective for these radars. In the case of the MMCRs these assumptions are problematic for the current ARM MMCR operational modes and, thus, the effectiveness of coherent integration is questionable for these radars.

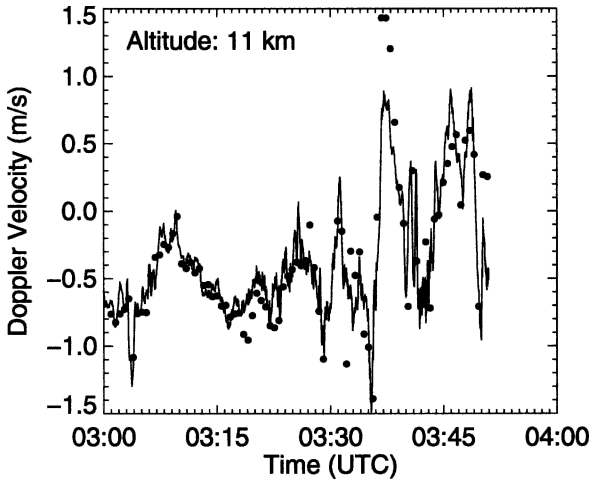

FIG. 10. Time series of mean Doppler velocity estimates from the ETL MMCR (dots) and the UM 94-GHz Doppler radar (solid line) generated within a cirrus cloud at 11 km of altitude.

6. Need for higher temporal resolution MMCR products

Certain assumptions about the nature and homogeneity of clouds were used during the design of the MMCR operational modes. For example, it was assumed that low-reflectivity clouds are composed of particles with terminal fall velocities no greater than 1–2 m s^{-1}. However, cloud particles in weakly reflecting clouds are potentially embedded within air parcels that are turbulent and have net vertical speeds. The extent of Doppler spectrum width broadening as a result of turbulence, as well as the range of vertical air motions in weakly reflecting clouds, was not rigorously assessed in the design of the original modes, largely because of a lack of observations. Consequently, the use of a large number of coherent integrations and long sampling periods T_s of 9 s were deemed acceptable in an attempt to maximize radar sensitivity.

Clouds are highly inhomogeneous with variable boundaries and sharp gradients in microphysical properties. Boundary layer clouds, in particular, can be highly turbulent as a result of their coupling with surface processes, with variability evident at all scales. As such, clouds cannot be treated as stationary targets over 9-s periods. The nature of the clouds not only affects the ability of radars to detect them, but also has a large impact on the quality of the Doppler moment estimates retrieved from them. We now assess how effectively the MMCRs capture cloud dynamics and morphology. In particular, we evaluate the effects of the long sampling interval T_s of 9 s and the narrow Nyquist velocity intervals of the current ARM MMCR operational modes when they are applied in the observation of clouds characterized by high turbulence.

During the CRYSTAL-FACE experiment conducted during July 2002, the ETL MMCR and UM 94-GHz Doppler radar (Albrecht and Kollias 1999) were collocated approximately 10 km southwest of downtown Miami, Florida. The UM cloud radar was operated with 30-m vertical resolution and 2-s temporal resolution. The observations from the UM cloud radar were used to characterize accurately the dynamical state of the clouds and to quantify the accuracy of the ETL MMCR operational sampling strategy. Consider the time series segment of mean Doppler velocity inside a cirrus anvil layer at 11-km altitude illustrated in Fig. 10. The comparison between the mean Doppler velocity estimates from the two radars shows good agreement when the temporal gradient in the mean Doppler velocity is small. After 0330 UTC, however, a generating cell near cloud top was sampled by the radars. Inside the generating cell the mean Doppler velocity magnitude increased and sharp horizontal gradients were observed. Because of its coarse temporal resolution and long signal dwell interval, the ETL MMCR filters the mean Doppler velocities and misrepresents the magnitude and frequency of the vertical air motions within the generating cell. Furthermore, as a result of the long sampling interval, the Doppler spectrum width estimates have contributions from horizontal shear in the vertical air motions at the altitude of the observations (Kollias et al. 2001), as well as from variability in the hydrometeor size distributions. Vertical air motion contributions to the Doppler spectrum widths make the interpretation of the Doppler spectrum width and its use in hydrometeor size distribution retrievals difficult.

Fair-weather cumulus clouds were particularly af-

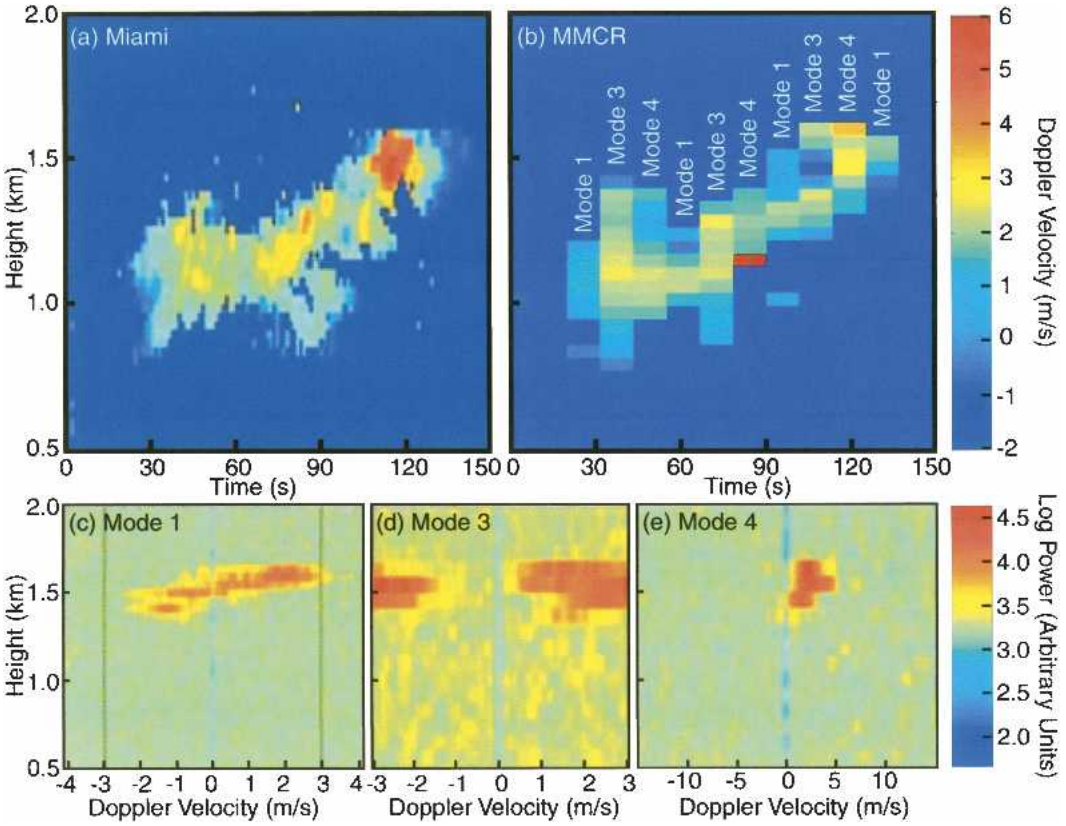

FIG. 11. Time vs height mappings of mean Doppler velocities from a single fair-weather cumulus cloud generated by (a) the UM 94-GHz Doppler radar and (b) the ETL MMCR. Three consecutive spectrograms from the ETL MMCR for (c) mode 1, (d) mode 3, and (e) mode 4 are shown at the bottom of the figure.

fected by the ETL MMCR operational sampling strategy. Besides their discontinuous and broken cloud field structures, fair-weather cumulus cloud interactions with surface processes make them highly turbulent. Time versus height mappings of the mean Doppler velocity field in a fair-weather cumulus cloud field obtained from the two radars during CRYSTAL-FACE are illustrated in Fig. 11. The fair-weather cumulus cloud field observations lasted almost 2 min. During that period the UM cloud radar collected 60 vertical profiles (Fig. 11a), while the ETL MMCR collected 10 profiles (Fig. 11b). Note that the ETL MMCR observations in Fig. 11b are the composite result of modes 1, 3, and 4. The cloud boundaries are well captured by the ETL MMCR, and only small details are smeared by the coarse temporal resolution of the ETL MMCR. The UM cloud radar mean Doppler velocity field shows distinct updraft cores within the cumulus cloud. The magnitude of the updraft velocities reached 6 m s^{-1}. Such velocities cannot be observed by the ARM MMCR boundary layer (mode 1) and general (mode 3) modes because their Nyquist velocities are 3 m s^{-1}. This is not the case for the robust mode (mode 4), which has a wide Nyquist velocity interval well over 10 m s^{-1}.

The problem with the ARM MMCR operational modes is exemplified 120 s into the time series when a strong updraft core, with a maximum velocity around 6 m s^{-1}, was observed by the UM cloud radar. During CRYSTAL-FACE, a wider Nyquist velocity interval of ± 4 m s^{-1} was implemented by ETL for mode 1, thereby improving the quality of the Doppler moment estimates and reducing velocity aliasing. The vertical lines in the ETL MMCR mode 1 Doppler spectra (Fig. 11c) show the Nyquist velocity interval of ± 3 m s^{-1} for mode 1 of the ARM MMCRs. For this period, the signal occupies a significant portion of the Doppler spectrum so that the coherent integration gain is reduced. As the recorded Doppler spectra from ETL MMCR mode 3 indicates (Fig. 11d), the narrow Nyquist velocity interval causes aliasing and the Doppler moment estimates are meaningless. Finally, as illustrated by the Doppler spectra collected by the robust mode (mode 4) (Fig. 11e), the Doppler spectra lie comfortably within the wide Nyquist velocity interval of mode

4 and the Doppler moment estimates are unbiased for this mode.

7. Summary

The MMCRs are one of the primary observing tools for the detection of nearly all radiatively important clouds over the DOE ARM sites. After years of operations at different locations around the world and comparisons with data from other remote sensors, the MMCRs have been shown to exhibit great sensitivity and fair operational stability. To assess the quality of the first three Doppler moment estimates, that is, radar reflectivity, mean Doppler velocity, and Doppler spectrum width, produced by the MMCRs, especially under low signal-to-noise ratios (SNRs), we evaluated MMCR Doppler moment estimates from all ARM sites in the context of a set of numerical simulations of the in-phase (i.e., I_t) and quadrature-phase (i.e., Q_t) radar signal voltages.

Overall, we found that errors are introduced into the Doppler moment estimates, especially at low SNRs, by the current operational modes. In particular, coherent integration in the current modes introduces biases into the radar reflectivity, mean Doppler velocity, and Doppler spectrum width estimates when either the mean Doppler velocity approaches the Nyquist velocity or the Doppler spectrum width is a significant fraction of the Nyquist velocity interval. The deleterious effects of coherent integration can be significantly reduced by decreasing the number of coherently integrated samples. To compensate for the increased Nyquist velocity and drop in velocity resolution, we can increase the number of points per FFT from 64–128 up to 512–1024 points. These changes are important if we intend to utilize the Doppler moment estimates in microphysical and turbulence retrievals.

We also analyzed the characteristics of ARM MMCR receiver noise. We found that the treatment of noise in the processing of the Doppler spectra to Doppler moments can produce biased noise mean power estimates under cloud conditions that lead to high SNR and broad Doppler spectrum widths. Errors in the noise mean power estimates result in biases in all of the Doppler moment estimates. Quality control criteria based on receiver noise power variance, SNR, and the Doppler moment estimates are suggested as a method to filter degraded Doppler moment estimates.

The performance of the ARM MMCR operating modes for cloud detection, cloud boundary estimation, cloud microphysical retrievals, and the characterization of turbulence was tested through comparisons with the Doppler moment estimates obtained from the University of Miami (UM) cloud radar during the CRYSTAL-FACE experiment. We found that the Doppler moments from the ETL MMCR and UM cloud radar were highly correlated, except in cases of high turbulence. Extension of the Nyquist velocity in the ETL MMCR boundary layer mode improved the Doppler moment estimates in fair-weather cumulus. However, the poor temporal resolution of the ETL MMCR degraded our ability to define precisely the cloud boundaries and the dynamical structure in shallow broken clouds when using this radar.

The temporal resolution of the current ARM MMCR operating modes severely limits our ability to study broken cloud field radiative effects and to produce reliable microphysical and turbulence retrievals. In addition, the narrow Nyquist velocity in three of the four ARM MMCR operational modes introduces biases into the Doppler moment estimates from these modes. To observe with fidelity eddies in boundary layer clouds, the sample interval of T_s of 9 s is much too coarse. Sampling intervals of 2 s or less are much more appropriate for cloud and turbulence studies. These findings will form the basis of the development of a new set of MMCR operational modes and quality assessment criteria not included in the current radar signal processing.

Acknowledgments. This research was supported by the Office of Biological and Environmental Research, Environmental Sciences Division, of the U.S. Department of Energy under Contract Numbers DE-FG02-97ER62337 and DE-FG02-90ER61071 as part of the Atmospheric Radiation Measurement program. Data were obtained from the Atmospheric Radiation Measurement program as well.

REFERENCES

Ackerman, T. P., and G. Stokes, 2003: The Atmospheric Radiation Measurement program. *Phys. Today*, **56,** 38–45.

Albrecht, B. A., and P. Kollias, 1999: Observations of Tropical Cloud Systems with a mm-wavelength cloud radar. An overview. Preprints, *29th Int. Conf. on Radar Meteorology,* Montreal, QC, Canada, Amer. Meteor. Soc., 454–456.

Clothiaux, E. E., M. A. Miller, B. A. Albrecht, T. P. Ackerman, J. Verlinde, D. M. Babb, R. M. Peters, and W. J. Syrett, 1995: An evaluation of a 94-GHz radar for remote sensing of cloud properties. *J. Atmos. Oceanic Technol.*, **12,** 201–229.

——, and Coauthors, 1999: The Atmospheric Radiation Measurements program cloud radars: Operational modes. *J. Atmos. Oceanic Technol.*, **16,** 819–827.

——, T. P. Ackerman, G. G. Mace, K. P. Moran, R. T. Marchand, M. A. Miller, and B. E. Martner, 2000: Objective determination of cloud heights and radar reflectivities using a combination of active remote sensors at the ARM CART sites. *J. Appl. Meteor.*, **39,** 645–665.

Dong, X., and G. G. Mace, 2003a: Profiles of low-level stratus cloud microphysics deduced from ground based measurements. *J. Atmos. Oceanic Technol.*, **20,** 42–53.

——, and ——, 2003b: Artic stratus cloud properties and radiative forcing derived from ground-based data collected at Barrow, Alaska. *J. Climate*, **16,** 445–461.

Doviak, R. J., and D. S. Zrnić, 1993: *Doppler Radar and Weather Observations.* 2d ed. 562 pp.

Frehlich, R. G., and M. J. Yadlowsky, 1994: Performance of mean-frequency estimators for Doppler radar and lidars. *J. Atmos. Oceanic Technol.*, **11,** 1217–1230.

Gordon, W. B., 1997: An effect of receiver noise on the measurement of Doppler spectral parameters. *Radio Sci.*, **32,** 1409–1423.

Hildebrand, P. H., and R. S. Sekhon, 1974: Objective determination of the noise level in Doppler spectra. *J. Appl. Meteor.*, **13,** 808–811.

Kato, S., G. G. Mace, E. E. Clothiaux, J. C. Liljegren, and R. T. Austin, 2001: Doppler cloud radar derived drop size distribution in liquid water stratus clouds. *J. Atmos. Sci.*, **58,** 2895–2911.

Kollias, P., and B. A. Albrecht, 2000: The turbulent structure in a continental stratocumulus cloud from millimeter wavelength radar observations. *J. Atmos. Sci.*, **57,** 2417–2434.

——, ——, R. Lhermitte, and A. Savtchenko, 2001: Radar observations of updrafts, downdrafts and turbulence in fair weather cumuli. *J. Atmos. Sci.*, **58,** 1750–1766.

Lhermitte, R., 1987: A 94-GHz Doppler radar for cloud observations. *J. Atmos. Oceanic Technol.*, **4,** 36–48.

——, and P. Kollias, 1999: Processing of millimeter wave Doppler signal in low signal to noise conditions. Preprints, *29th Int. Conf. on Radar Meteorology,* Motreal, QC, Canada, Amer. Meteor. Soc., 517–520.

Lottman, B. T., and R. G. Frehlich, 1997: Evaluation of Doppler radar velocity estimators. *Radio Sci.*, **32,** 677–686.

Luo, Y., S. K. Krueger, G. G. Mace, and K.-M. Xu, 2003: Cirrus cloud properties from a cloud-resolving model simulation compared to cloud radar observations. *J. Atmos. Sci.*, **60,** 510–525.

Mace, G. G., E. E. Clothiaux, and T. P. Ackerman, 2001: The composite characteristics of cirrus clouds: Bulk properties revealed by one year of continuous cloud radar data. *J. Climate*, **14,** 2185–2203.

Moran, K. P., B. E. Martner, M. J. Post, R. A. Kropfli, D. C. Welsh, and K. B. Widener, 1998: An unattended cloud-profiling radar for use in climate research. *Bull. Amer. Meteor. Soc.*, **79,** 443–455.

Sassen, K., G. G. Mace, Z. Wang, M. R. Poellot, S. M. Sekelsky, and R. E. McIntosh, 1999: Continental stratus clouds: A case study using coordinated remote sensing and aircraft measurements. *J. Atmos. Sci.*, **56,** 2345–2358.

Schmidt, G., R. Ruster, and P. Czechowsky, 1979: Complementary code and digital filtering for detection of weak VHF radar signals from the mesosphere. *IEEE Trans. Geosci. Electron.*, **17,** 154–161.

Sirmans, D., and B. Bumgarner, 1975: Numerical comparisons of five mean frequency estimators. *J. Appl. Meteor.*, **14,** 991–1003.

Spinhirne, J. D., R. Boers, and W. D. Hart, 1989: Cloud top liquid water from lidar observations of marine stratocumulus clouds. *J. Appl. Meteor.*, **28,** 81–90.

Stokes, G. M., and S. E. Schwartz, 1994: The Atmospheric Radiation Measurement (ARM) Program: Programmatic background and design of the Cloud and Radiation Test Bed. *Bull. Amer. Meteor. Soc.*, **75,** 1201–1222.

Vali, G., R. D. Kelly, J. French, S. Haimov, D. Leon, R. E. McIntosh, and A. Pazmany, 1998: Finescale structure and microphysics of coastal stratus. *J. Atmos. Sci.*, **55,** 3540–3564.

Zrnic, D. S., 1975: Simulation of weatherlike Doppler spectra and signals. *J. Appl. Meteor.*, **14,** 619–620.

——, 1979: Estimation of spectral moments for weather echoes. *IEEE Trans. Geosci. Remote Electron.,* **GE-17,** 113–128.